JACS
JOURNAL OF THE AMERICAN CHEMICAL SOCIETY
pubs.acs.org/JACS
Article

Off-Stoichiometric Restructuring and Sliding Dynamics of Hexagonal Boron Nitride Edges in Conditions of Oxidative Dehydrogenation of Propane

Zisheng Zhang, Ive Hermans, and Anastassia N. Alexandrova*

Cite This: J. Am. Chem. Soc. 2023, 145, 17265−17273
Read Online

ABSTRACT: Boron-containing materials, such as hexagonal boron nitride (h-BN), recently shown to be active and selective catalysts for the oxidative dehydrogenation of propane (ODHP), have been shown to undergo significant surface oxyfunctionalization and restructuring. Although experimental ex situ studies have probed the change in chemical environment on the surface, the structural evolution of it under varying reaction conditions has not been established. Herein, we perform global optimization structure search with a grand canonical genetic algorithm to explore the chemical space of off-stoichiometric restructuring of the h-BN surface under ambient as well as ODHP-relevant conditions. A grand canonical ensemble representation of the surface is established, and the predicted ^{11}B solid-state NMR spectra are consistent with previous experimental reports. In addition, we investigated the relative sliding of h-BN sheets and how it influences the surface chemistry with ab initio molecular dynamics simulations. The B−O linkages on the edges are found to be significantly strained during the sliding, causing the metastable sliding configurations to have higher reactivity toward the activation of propane and water.

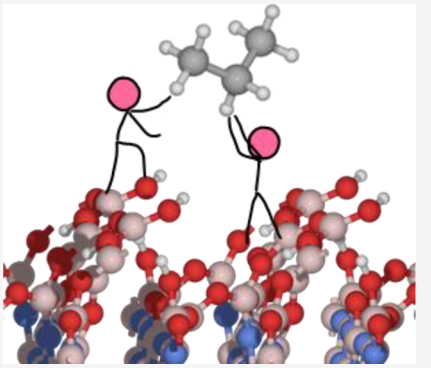

INTRODUCTION

The conversion of light alkanes to olefins—such as propane to propylene—is an important industrial process that currently requires high energy input.[1] Introducing more efficient and cost-effective catalysts for the exothermic oxidative dehydrogenation reaction can reduce energy consumption, improve sustainability and lower the environmental impact of light alkene production.[2] Out of a serendipitous discovery, a family of boron-containing compounds has been reported to show surprisingly high activity and selectivity for the oxidative dehydrogenation of propane (ODHP).[3,4] The most intriguing material among them is hexagonal boron nitride (h-BN), which is metal-free and comprised of rather inert chemical bonds.

Experimental efforts have been made to understand the origin of h-BN's catalytic activity. A common denominator among all boron-containing OHDP catalysts is the formation of a boron oxide/hydroxide layer, for instance, observed by comparing the B 1s XPS or ^{11}B NMR spectra of the fresh and spent catalyst.[4] Moreover, the active species should consist of extended >B−O−B< linkages or networks, while the isolated boron sites seem inactive.[5] All evidence so far points to the formation of a boron oxide/hydroxide layer over the catalyst surface under ODHP conditions being responsible for the catalysis. However, the as-formed boron oxide/hydroxide layers are amorphous and non-stoichiometric, making it hard to establish realistic models of the boride/oxide interface and to understand the exact structure of the active sites.

The reaction system is further complicated by the possible role of metastable species only accessible at the reaction conditions.[6] The h-BN face has been predicted to reconstruct into a large number of surface states under ODHP conditions, which coexist and interconvert on the timescale of a few picoseconds, requiring a statistical ensemble representation.[7] The "hot sites", which only gain significant population under the catalytic conditions, contain uncommon structural motifs such as unsaturated B−B−B linkage and dangling terminal >B−O, which have been experimentally probed as the key species in promoting a surface-initiated radical chemistry that propagates in the gas phase to do the majority of the turnover.[8,9]

The hydroxylated edges of the h-BN, which have been probed by ^{11}B solid-state NMR (SSNMR),[10] have also been proposed as the key active species for ODHP. However, those characterizations were ex situ and could only inform about the local connectivity. The time-averaging nature of the measure-

Received: May 4, 2023
Published: July 28, 2023

https://doi.org/10.1021/jacs.3c04613
J. Am. Chem. Soc. 2023, 145, 17265−17273

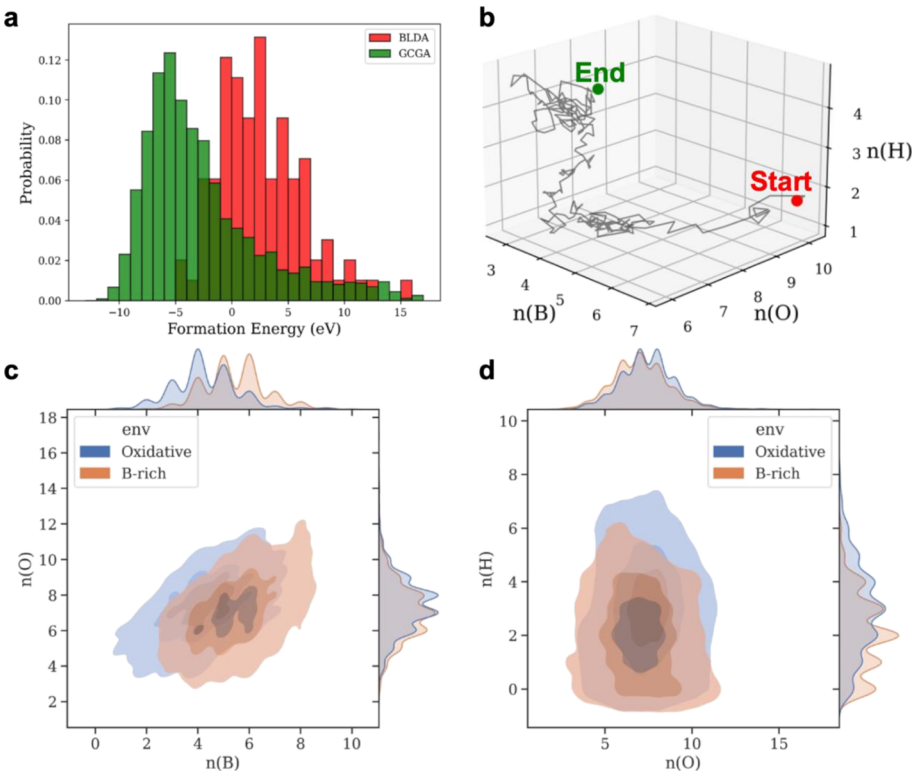

Figure 1. Sampling distributions of the GCGA searches. (a) Comparison of the sampling efficiencies of GCGA and random sampling by DLBA. (b) Evolution of the population averaged in the compositional space during a GCGA search. Projections of the GCGA sampling density plot in (c) plane defined by a number of B and O and (d) plane defined by a number of O and H, with the samples from two searches at different sets of chemical potential overlapped.

ments also risks overwhelming the signal of metastable states (of low population but high activity) by signals of the bulk or the most stable surface phase. To this date, there has been no systematic exploration of the stable or metastable edge restructuring configurations under ODHP-relevant conditions.

In this work, we present a grand canonical genetic algorithm (GCGA), a global optimization strategy specialized for off-stoichiometric restructuring surfaces, and apply it to study the armchair and zigzag edges of h-BN under relevant conditions to ODHP. The sampling results are used to construct statistical grand canonical ensemble representations and surface phase diagrams of the edges. The ensemble representations help interpret the shift and trend of key signals of ^{11}B SSNMR in the previous report. The data of diverse structures generated during the GCGA can naturally serve as the training set for machine learning (ML) models, enabling low-cost and accurate prediction of ^{11}B chemical shifts, atomic charges, and surface energy. We also investigated the dynamics of sheet sliding and how it influences the chemistry on the restructured edges of h-BN.

COMPUTATIONAL METHODS

Model Setup. The armchair edge of h-BN is modeled by a 5-atomic-layer 2 × 2 slab with a cell dimension of 6.69 Å × 8.69 Å. The bottom of the slab is capped by H to saturate the dangling bonds. The bottom 4 atomic layers are constrained as the bulk region, and everything else is allowed to relax as the interface region. The zigzag edge of h-BN is modeled by a 6-atomic-layer 2 × 2 slab with a cell dimension of 7.53 Å × 6.69 Å. The bottom of the slab is capped by H to saturate the dangling bonds. The bottom 5 atomic layers are constrained as the bulk region, and everything else is allowed to relax as the interface region. A vacuum slab of 15 Å thickness is added to all asymmetric slab models in the Z direction to avoid spurious interactions between periodic images.

Density Functional Theory (DFT) Calculations. The local optimizations and energy evaluations are performed with the PBE functional[11] and PBE_PAW pseudopotentials[12] using the VASP program (version 5.4.4).[13−16] The D3 correction is added to improve the description of dispersion interactions. Spin polarization is used for all DFT calculations throughout the global optimization process with an initial magnetic moment of 1 for each atom, which we assume to yield the correct ground state for each sampled configuration. The dipole correction is added to eliminate dipole effects caused by the asymmetric slab. The convergence criteria for electronic and force minimization are set to 10^{-5} eV and 0.02 eV/Å during the global optimization. Due to the large amount of sampling needed, only the Γ k-point is sampled in the reciprocal space of the Brillouin zone throughout, and the cutoff energy for the kinetic energy of the plane waves is set to 400 eV.

The transition states (TS) are located using the climbing image nudged elastic band method[17] with image-dependent pair potential interpolation.[18] Each TS geometry has been confirmed to have only one imaginary mode. All electronic structure analyses are performed based on converged charge density or wavefunction. The Bader charges are calculated from the charge densities using the Bader charge analysis program.[19] The chemical shift tensors are calculated by VASP with a more accurate setting (PREC = accurate) based on the locally optimized geometries (see Figure S3 for the benchmarking).

The ab initio molecular dynamics (AIMD) simulations are performed on minima structures with the same DFT setting as the geometry optimization using the VASP program. The simulation is performed in the *NVT* (canonical) ensemble at 300 K with the Nose−Hoover thermostat. The time step is set to 1 fs and a 10 ps trajectory after the equilibration of the system is collected for analysis. Clustering analysis is performed using the Python module, GOCIA.

https://doi.org/10.1021/jacs.3c04613
J. Am. Chem. Soc. 2023, 145, 17265−17273

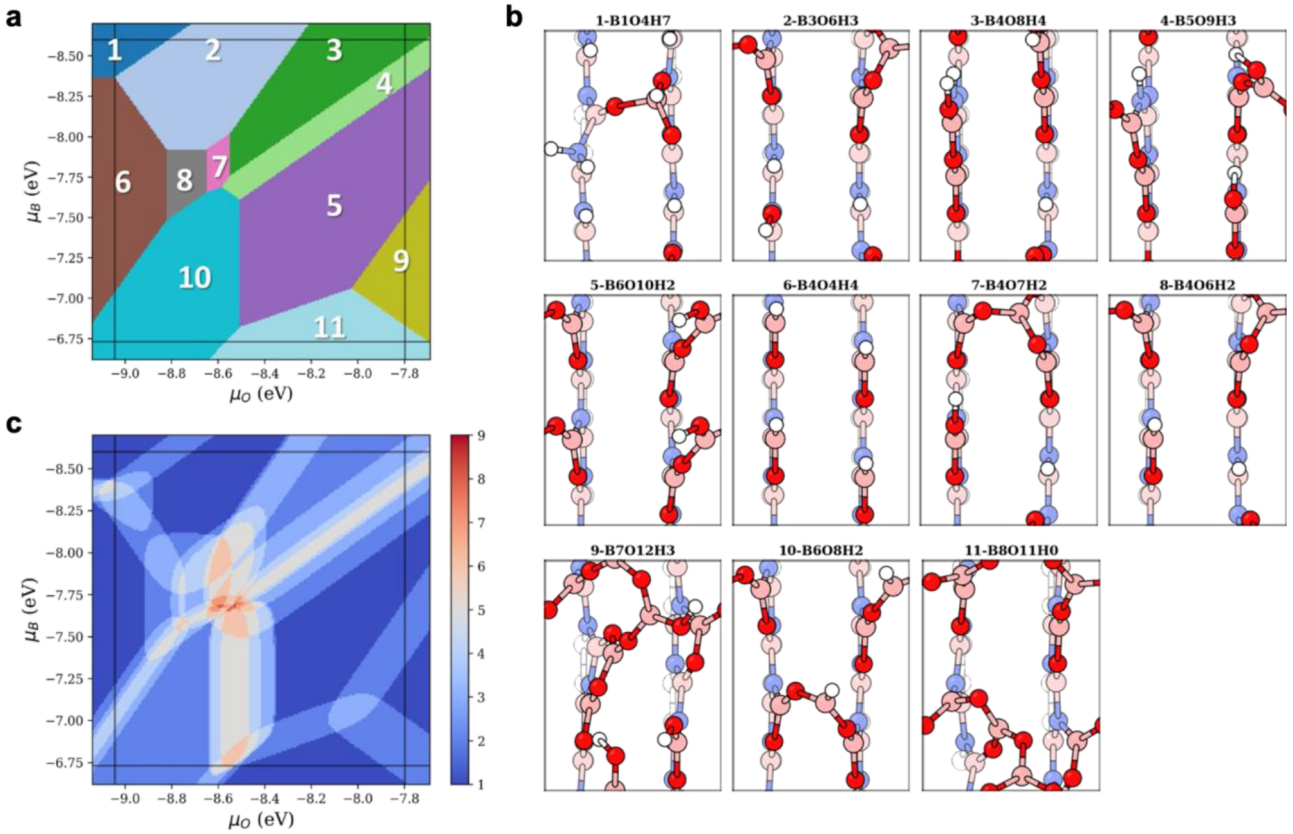

Figure 2. Surface phase diagram of h-BN armchair edge. (a) Surface phase diagram of only the global minimum states, as a function of μ_B and μ_O. (b) Top views of corresponding structures, with white, pink, and red spheres representing H, B, and O, respectively. (c) Surface phase diagram showing the number of "hot" surface states, i.e., the ones that only gain a >5% population when heated above 763 K, as a function of μ_B and μ_O.

Grand Canonical Genetic Algorithm Global Optimization. To explore the vast chemical space of amorphous and off-stoichiometric restructuring of extended surfaces and to obtain the global minimum (GM) and all relevant local minima (LM), we perform global optimization minima search using the GCGA implemented in our open-source Python module, GOCIA. With this approach, we do not need to grid-search every possible stoichiometry, and we can relax the composition of the system with the search target being the grand canonical free energy:

$$\Omega = E(^*B_xO_yH_z) - \sum_i^{B,O,H} \mu_i N_i$$

Here, $E(^*B_xO_yH_z)$ is the DFT-calculated energy of a surface state with an overlayer of the composition, $B_xO_yH_z$. The μ's are chemical potentials of B, O, and H in the reservoir, which can exchange atoms with the sampling region of the system during the search. The N's are numbers of B, O, or H atoms in the sampling region. The choice of μ, which is a function of the energetics of key species and experimental conditions (temperature, partial pressure, etc.), is detailed in Supplementary Note 1.

A population size of 30 and a mutation rate of 30% are chosen for the GCGA sampling. The pool of initial candidates is generated using the bond-length distribution algorithm (BLDA), which is a random structure generation method based on the covalent radii of the atoms.[20] A pre-optimization with Hookean potential is performed to produce reasonable starting geometries before they are fed to electronic structure codes for local optimization and energy evaluation. Mating between the alive candidates to create offspring by the split-and-splice operation,[21] in which the parent slabs are cut along a random plane and then spliced together. The fitness factor is assigned to each candidate based on the grand canonical free energy. An over-mating penalty factor of $(1 + N_{mate})^{-3/4}$, where N_{mate} is the mating counts, is multiplied to the fitness factor. Candidates with higher fitness are more probable to mate. Similarity checks against the current population are performed before adding any new candidate to remove duplicates. Adopted mutation operations include (1) adding or removing an atom, (2) rattling the surface atoms along random vectors drawn from a normal distribution, (3) translating the buffer slab along the x or y axis by one-half of the cell length, and (4) permuting a random half of buffer slab. If an offspring is too similar to its parent, its mutation rate is raised to 100% to avoid recalculating the same structure. Upon the addition of each offspring to the population, the candidate with the lowest fitness is archived to maintain the population size.

The nature of GCGA search makes its resulting ensemble a naturally diverse (in structure and composition) dataset, which is suitable for training ML models. We made random forest (RF) models using the scikit-learn Python module for prediction of surface energy, Bader charge, and ^{11}B chemical shift.[22] The dataset is randomly divided into training set (2/3) and testing set (1/3) for validation purposes. Details of the model and features are discussed in Supplementary Note 2.

RESULT AND DISCUSSION

The oxidation and hydroxylation of h-BN terminations span a vast chemical space rich in LM regions. To obtain all the ODHP-relevant minima efficiently, we use the GCGA to search minima of armchair and zigzag edges of h-BN under four sets of conditions corresponding to pre/post-reaction and with/without propane.

In total, 5862 and 4726 unique structures are obtained for the armchair and zigzag edges, respectively. The GCGA sampling shows a superior sampling efficiency in locating the low-energy minima as compared to the one-shot random sampling by the BLDA, as is shown by the distribution of

https://doi.org/10.1021/jacs.3c04613
J. Am. Chem. Soc. 2023, 145, 17265−17273

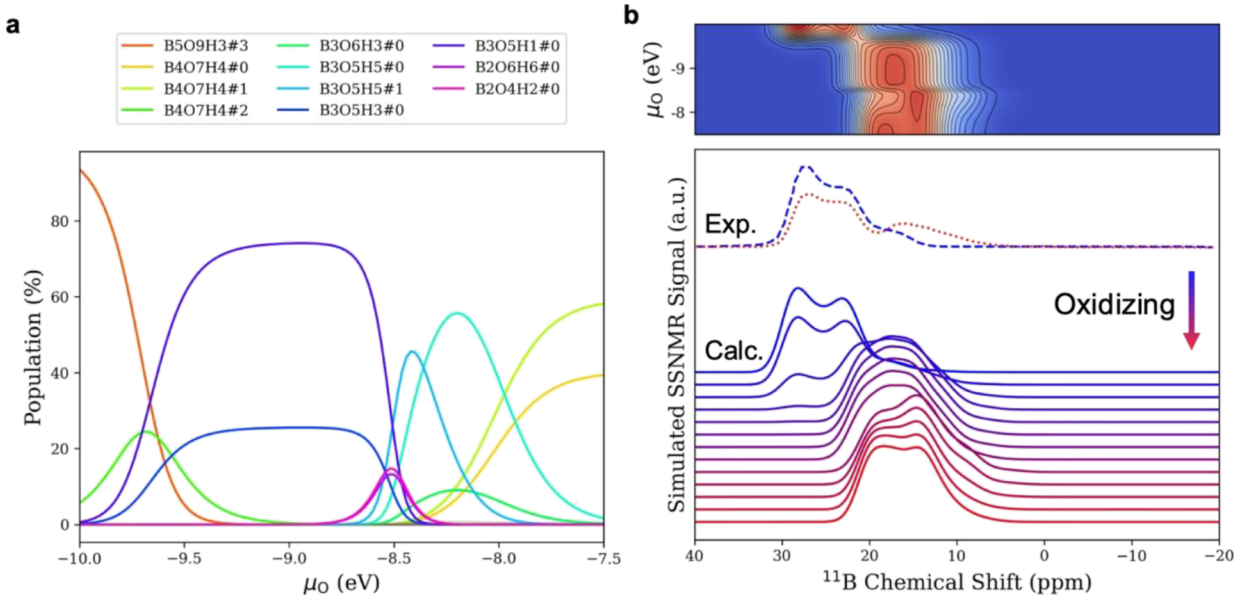

Figure 3. Ensemble-based simulation of ^{11}B SSNMR spectra for the h-BN armchair edge. (a) Evolution of population of accessible surface phases as a function of μ_O. The $B_xO_yH_x\#n$ denotes the nth local minima (zeroth is the global minimum) of the surface stoichiometry of $B_xO_yH_z$. (b) Evolution of ^{11}B SSNMR spectra as a function of μ_O. The experimental data from ref 23 are also shown in the lower panel for comparison. Adapted from ref 23. Copyright 2019 American Chemical Society.

samples in Figure 1a. During the GCGA search, the population updates its search direction in the compositional space adaptively according to the fitness of the alive candidates, making its way toward the GM region while sampling relevant compositions along the way (Figure 1b), with weak dependence on the initial population. The efficient sampling leads to a rather wide distribution of compositions in the final ensemble, with significant sampling density in the range of $B_{1-7}O_{3-12}H_{0-7}$ (Figure 1c,d). When the reference chemical potentials are changed, the sampling distribution also shifts accordingly to cover a different range of compositions. By merging the samples from the two extreme conditions, the fresh B-rich condition and the catalytic oxidative condition, the resulting ensemble would well cover all stoichiometries relevant to the interpolated regions between the two sampled conditions.

Thereby, we could construct the surface phase diagram, completely from first principles, based on the obtained samples, by reweighing the states according to their grand canonical free energy at each set of chemical potentials by Boltzmann statistics. Figure 2a shows the phase diagram based on the most thermodynamically stable surface states of the armchair edge in the ODHP-relevant ranges of μ_B and μ_O, with the top view of each notable surface phase shown in Figure 2b. The μ_B depends on the amount of excess B precursor left on the terminations from the synthesis, and the μ_O reflects how oxidative the reaction condition is. At ambient conditions, the h-BN armchair edge regions with low excess B (phase 1—$B_1O_4H_7$) tend to be capped by H to form N−H and B−H terminals, with a small amount of O to form the BO_3 motif bridging between the adjacent h-BN sheets; in regions with high excess B, the edge (phase 10—$B_6O_8H_2$) would be mildly oxidized, with B−O bonds closing the hexagons at the direct h-BN/oxide interface and reductive B−H terminals sticking out on the top surface. Under an oxidizing condition, the armchair edge regions with low excess B (phase 3—$B_4O_8H_4$) tend to grow BO_2(OH) motifs along the plane of the h-BN sheet; however, the regions with high excess B (phase 11—$B_8H_{11}H_0$) would form a thick B_2O_3-like overlayer. Since the B_2O_3 overlayer can partially screen the direct h-BN surface from the gas phase, and the majority of the terminations have a moderate amount of excess B, the effective μ_O and μ_B would fall in the middle region enclosed by the extrema, mostly forming partial oxide/hydroxide layers bridging between adjacent sheets. Note that there is not just one phase under each specified condition, but multiple phases. Each phase behaves like a hyperplane in the phase space, with multiple phases overlaying and intersecting each other over the whole range of relevant chemical potentials. As temperature increases to the reaction temperature, 763 K, the population distribution of surface states broadens, and some low-energy metastable states would gain a significant population and become accessible, which we dub as "hot" states. Figure 2c shows the number of "hot" states (population gain cutoff: >5%) as a function of reaction conditions. The number of "hot" states is larger at the inter-phase boundaries, especially, the regions of moderate μ_O and μ_B, which corresponds to the local environment of the majority of the edge, have up to 9 coexisting "hot" states.

The scenario is similar on the zigzag edge (Figure S3), but with less tendency to form bridging BO_3 between adjacent h-BN sheets, likely due to the mismatch in height of the terminal B atoms on adjacent sheets (from the AB stacking pattern) and the stabilization of in-plane terminal B−OH groups by hydrogen bond interactions (e.g., phases 3, 4, and 7 in Figure S3).

One can take a slice of the surface phase diagram and look at the evolution of state populations as a function of varying conditions. Figure 3a shows the evolution of surface phase populations on the armchair edge of h-BN as the condition becomes more oxidizing (geometries of mentioned surface phases are in Figure S4). Experimentally, this would correspond to running the reaction from oxygen lean to rich, or high oxygen consumption at the outlet of a flow reactor to low oxygen conversion at the inlet of the reactor. Multiple

https://doi.org/10.1021/jacs.3c04613
J. Am. Chem. Soc. 2023, 145, 17265−17273

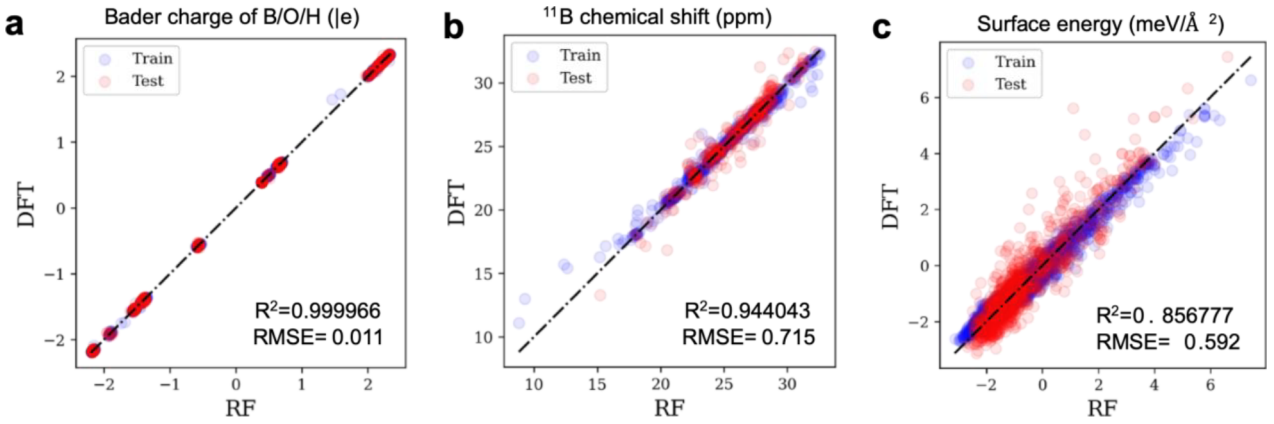

Figure 4. Accuracy of predictive machine learning models trained on the GCGA samples. Parity plots of (a) Bader charge prediction for B, O, and H, (b) ^{11}B chemical shift prediction, and (c) surface energy prediction using the trained random forest models.

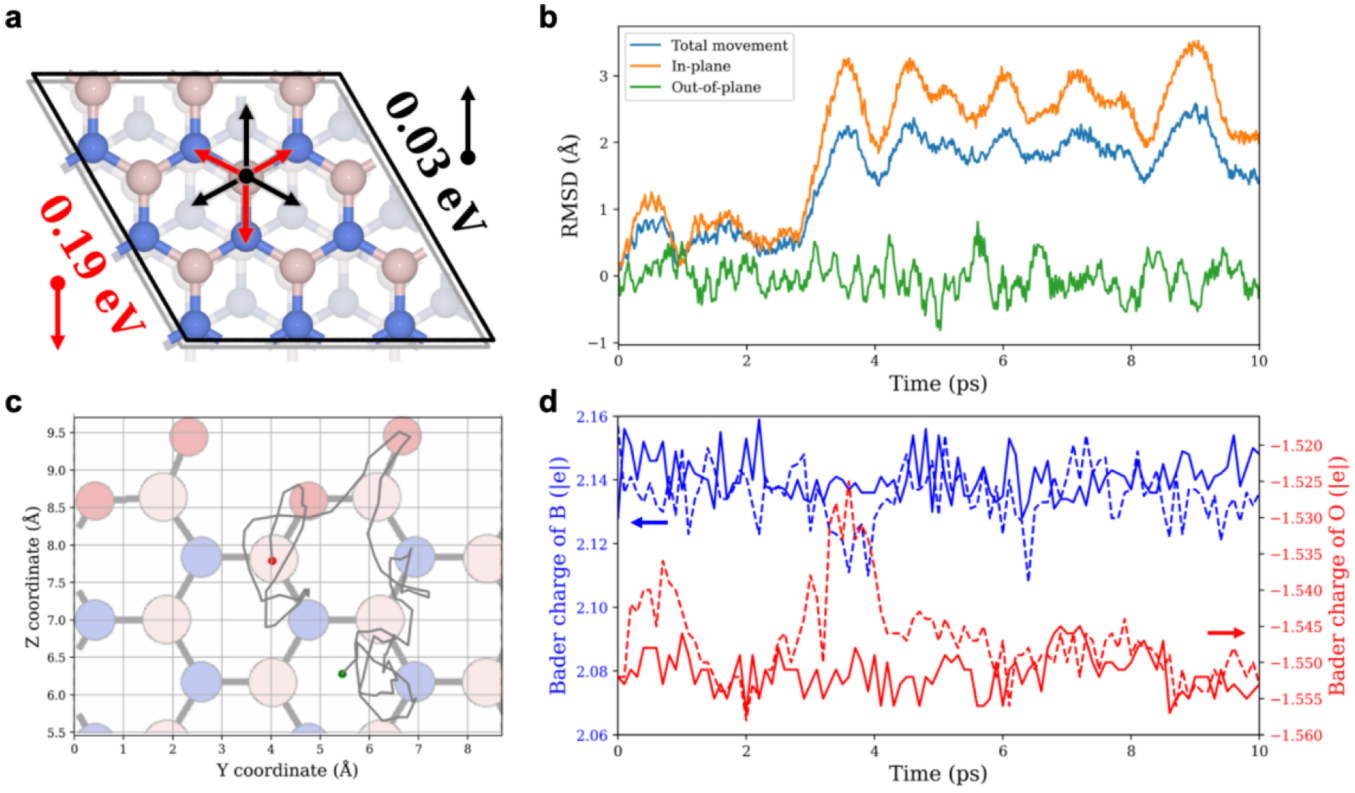

Figure 5. Sliding dynamics of h-BN sheets. (a) Energy barriers of sheet sliding in different directions, calculated from the h-BN bulk structure. (b) Root-mean-square deviation of a free h-BN sheet during the AIMD simulation, decomposed into in-plane and out-of-plane movements. (c) Sliding path of a free h-BN sheet during the AIMD simulation, with red and green dots marking the start and end points, respectively. (d) Evolution of Bader charge of B and O in the bridging linkage during the AIMD simulation. The curves of free and fixed sheets are plotted as dashed and solid lines, respectively.

surface phases of different stoichiometries can coexist, and there are several metastable phases with significant populations. The grand canonical ensemble representation enables the simulation of ensemble-averaged spectra of a specific spatial region under varying conditions. Figure 3b shows the ensemble-averaged ^{11}B SSNMR spectra of the top surface only, as the condition becomes more oxidizing. In the beginning, the major peak is at ca. 30 ppm, corresponding to B−N linkages on h-BN edges that are not oxyfunctionalized. At mild oxidative conditions, the B−N signals decrease, and a shoulder peak forms at ca. 19 ppm, corresponding to B−O linkages. At more oxidative conditions, the B−N signals on the surface layer are completely gone, and the 19 ppm peak dominates as the edge gets further oxyfunctionalized and hydroxylated, and a ca. 10 ppm shoulder peak corresponding to boron oxide is formed. The scenario is similar for the zigzag edge (Figures S5 and S6), with only a minor difference in the peak shape (corresponding to the ratio of different motifs with similar chemical shifts). The simulated ^{11}B SSNMR spectra and the trend under varying conditions agree well with previous experimental reports[23] and provide detailed structural insights of the surface-only region, which are derived completely from first principles. It is noteworthy that the armchair edge is more easily oxidized than the zigzag edge, as is characterized by the onset μ_O

https://doi.org/10.1021/jacs.3c04613
J. Am. Chem. Soc. 2023, 145, 17265−17273

beyond which oxidation begins (ca. −9.6 eV for the armchair edge and ca. −8.7 eV for the zigzag edge), due to the different reactivity of their terminal motifs. Other more complex terminations of h-BN may also have slightly different oxidizability, resulting in a step-wise activation stage of the h-BN before all its surface regions transform to catalytic phases toward ODHP.

The ensemble constructed from GCGA samplings has been shown to contain a wide variety of structural motifs that are relevant to ODHP conditions. This makes a large and diverse dataset spanning the whole chemical subspace of interest, which is naturally suitable as a training set for ML models. Here, we train RF models, with the structural descriptors proposed by ref 24, on the ensembles to predict the Bader charge, SSNMR chemical shift and surface energy of off-stoichiometric restructured h-BN edges (Figure 4). The accuracy of Bader charge prediction for B, O, and H is high, with R^2 of 0.99997 and root mean square error (RMSE) of only 0.011 |e|. The prediction of ^{11}B chemical shift is also accurate, with R^2 of 0.944 and RMSE of 0.715 ppm, likely due to the higher sensitivity of the shielding to local structural patterns. The surface energy prediction is less satisfactory, with R^2 of 0.857 and RMSE of 0.592 meV/Å^2, but it can still serve as a low-cost filter during global optimization search.

Although, experimentally, a variety of borides and boron-containing materials function as ODHP catalysts, h-BN remains one of the most active ones. Having established a detailed understanding of the off-stoichiometric restructured h-BN edges, we now further investigate what sets h-BN apart from other borides. We note that, while metal borides are mostly structurally rigid, and some are super-hard, the layered h-BN structure consists of two-dimensional (2D) sheets held together by $\pi - \pi$ stacking interactions. The material is thus prone to sheet sliding, featuring a flat potential energy surface (PES) and periodically distributed "sliding minima" separated by low barriers of 0.03 or 0.19 eV, depending on the sliding direction (Figure 5a). We hypothesize that this leads to the enhanced ODHP activity. Since the ODHP catalysis takes place at higher temperatures, we expect the sheets to slide dramatically and access multiple sliding minima, which can compress or stretch the surface boron oxide/hydroxide layer, as it is bridging the adjacent sheets. To explore the possible effect on the reactivity, we focus on phase 4—$B_5O_9H_3$ of the armchair edge (Figure 2b) in the following, and start by performing the AIMD simulation of a four-sheet supercell of it (two layers fixed and two layers free to slide) at 763 K in the *NVT* ensemble. The RMSD of a free-to-slide sheet is shown in Figure 5b. It is obvious that the sheet does not move much in the out-of-plane direction but moves dramatically in the in-plane directions. By tracking the movement of the sheet in Figure 5c, we can see that the sheet can slide and access multiple sliding minima in the timescale of a few picoseconds. As the sheet slides around, the bridging boron oxide/hydroxide linkages are strained along the way, leading to a much higher fluctuation of the B−O−B angle, O−B−O angle, and O−B−O−B dihedral angle of those bridging linkages (Figure S7a−c). In addition to enhanced geometric fluctuations, there are also larger fluctuations in the electronic structure of the B−O linkages, as is reflected by the evolution of the Bader charge of the B and O in the bridging linkages (Figure 5d) on the free sheet than on the fixed sheet, quantified by standard deviations in Figure S7d,e.

The pronounced fluctuation in Bader charges solely from bending and torsion of the B−O bonds originates in the anisotropic nature of the B−O bond. As is shown in Figure 6,

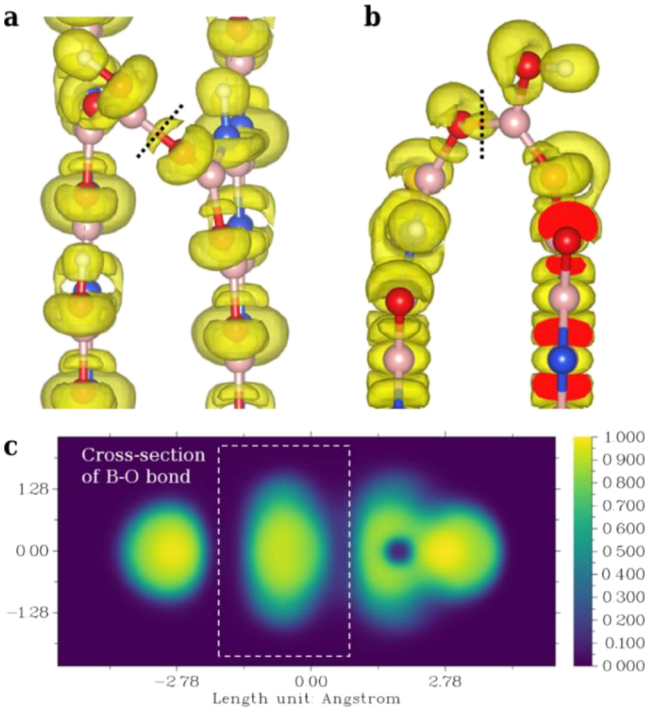

Figure 6. Chemical bonding analysis of the B−O bond. The isosurfaces of electron localization function (ELF) at an isovalue of 0.825 for phase 4 of the armchair edge, (a) top and (b) side view. (c) Colormap showing the ELF of the cross-section plane of the B−O bond marked in the isosurfaces.

the electron localization function of the B−O bond cross-section plane shows an elliptic shape, which suggests significant π characteristics in the BO_3 motif (as compared to the perfect circle shape of σ bond cross-section). As the h-BN sheets slide relative to each other, the π characteristics of the B−O bonds change along with the bending and torsion of the B−O linkages, leading to changes in the bond strength and redistribution of charge. In other words, the sliding of h-BN sheets can solely populate an ensemble of sliding configurations of different geometric and electronic structures, even for a surface phase of constant composition and connectivity. This effect is inaccessible to other, more rigid borides.

To further investigate how the distortion of bridging linkages from sliding influences their reactivity, we first locate the relevant low-energy sliding configurations by annealing from the AIMD trajectory. Note that there can be more accessible sliding configurations under the reaction condition, but here we focus on the three interconverting ones to probe the sliding effects on reactivity. Figure 7a shows the energy diagram of interconversion and geometries of the three sliding configurations of the lowest energies. The presence of bridging linkage slightly reshapes the PES of h-BN sheet sliding, breaking the degeneracy of the energy of the sliding minima and raising the barriers (compared to the 0.03 eV barrier of a similar sliding direction in Figure 5a). The higher energy a sliding configuration has, the more strained its bridging linkage is, i.e., likely more activated. Indeed, the barriers for propane activation on the bridging B−O of those sliding configurations

https://doi.org/10.1021/jacs.3c04613
J. Am. Chem. Soc. 2023, 145, 17265−17273

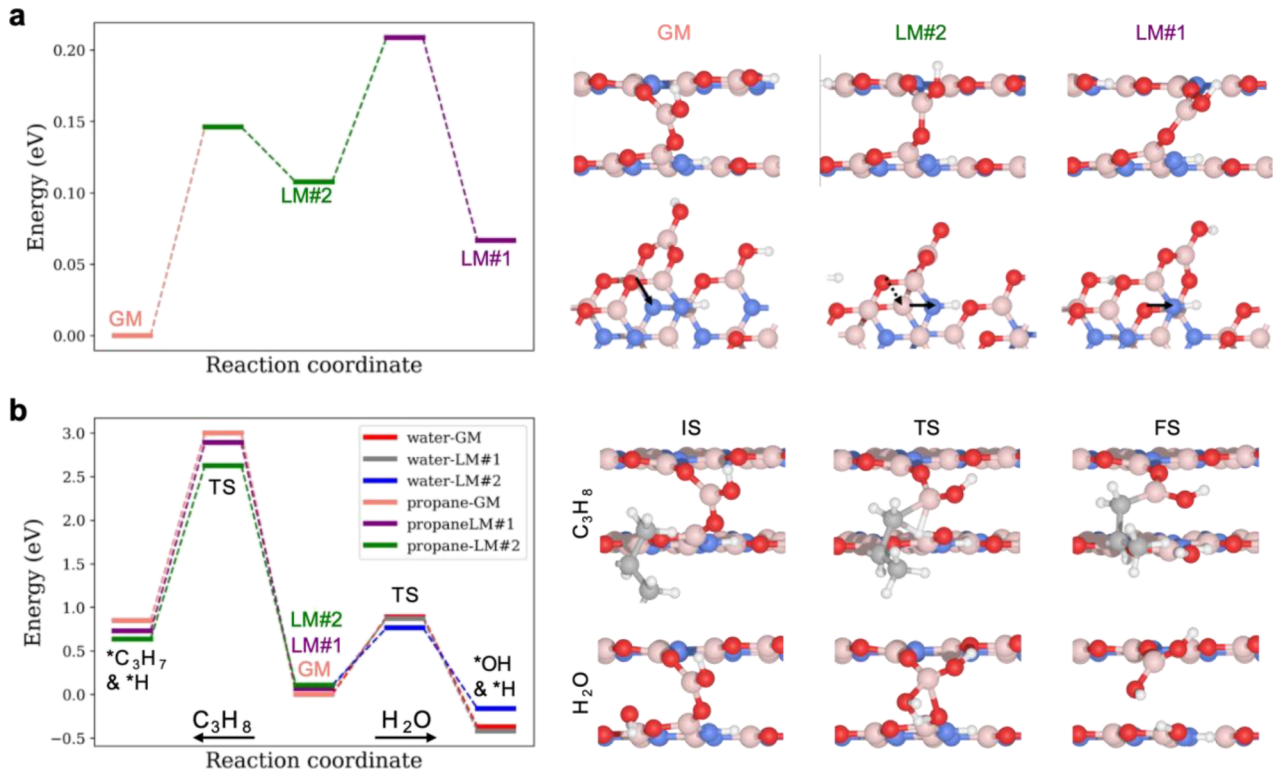

Figure 7. Influence of the sheet sliding on the reactivity of bridging linkages at the h-BN edge. (a) Energy diagram of a restructured h-BN armchair edge, phase 4 as in Figure 2, interconverting among the three sliding configurations of the lowest energy. (b) Energy diagram of water activation (from center to right) and propane activation (from center to left) on the bridging B−O of the three sliding configurations. Corresponding geometries are shown on the right side of each energy diagram.

follow an inverse order from that of their energies, that is, the GM has the highest barrier, whereas the second LM (LM#2) has the lowest barrier (Figure 7b). In addition, the absolute energy of the TS for propane activation is the lowest for LM#2 and the highest for GM, indicating the rate contributions to be GM < LM#1 < LM#2 (1:5:287, estimated by Arrhenius law) despite the lower population of LM#2 (Boltzmann population: 8.3% at 300 K and 17.4% at 800 K). The trends in barrier and absolute energy of the TS are similar for water activation on the three sliding configurations, with LM#2 being the most reactive and GM being the least. Note that here we aim to probe the effect of sliding dynamics on reaction barriers on only one specific site, and there surely can be active sites and pathways of lower barriers. Although not explicitly investigated herein, we believe that such promoting effects are universal to other bridging linkages, as the sliding coordinate is orthogonal to the reaction coordinate in the conventional view. Hence, the above discussion of sliding effects on bonding and reactivity should still hold true regardless of the detailed structure of the active site or the activated complex, as long as the reactive site can be strained by sliding dynamics.

The above analysis assumes that the sliding configuration stays the same during the course of the reaction. However, the reality can be far more complicated: the sliding can take place in a similar or shorter timescale than the ODHP reaction steps. In that case, the reaction coordinates of sliding and ODHP would weave into a 2D free energy landscape where the two events can be step-wise (L-shaped path) for some initial configurations and coupled (diagonal path) for others. Those coupled pathways, if accessible, could have even lower barriers, resulting in a higher overall activity. Either way, we expect the exceptional OHDP activity of h-BN to stem from its flexible B−N skeleton and mobile layered structures, as compared to the metal borides whose bulk structure is rigid and not capable of similar sliding dynamics.

CONCLUSIONS

In this work, we developed a GCGA workflow for efficient minima search of off-stoichiometric restructuring surface structures at the DFT level. The method is used to construct a grand canonical ensemble representation of the h-BN armchair and zigzag edges under ODHP conditions. Based on the ensemble representation, we explore the evolution of surface phases under varying conditions, from ambient to oxidation environments. Our simulated ensemble-averaged ^{11}B SSNMR spectra are in excellent agreement with previous experimental reports and provide a detailed atomistic understanding of the chemical transformations during the catalyst activation process. In addition, we show that the samples from grand canonical global optimization can serve as a structurally diverse dataset for training data-driven models for predictive tasks. We probe the sliding dynamics of h-BN sheets under reaction temperature by AIMD simulations, which turned out to be rather mobile and is able to slide on the timescale of a few picoseconds. The sliding dynamics is found to populate an extended ensemble of sliding configurations for each surface phase, causing a strain on the boron oxide/hydroxide surface layer. The distortion of the bridging B−O linkages is apparently able to activate them for propane and water activations, with the metastable sliding configurations showing higher activity than the most stable configuration. We hypothesize such sliding-enhanced reactivity to be the origin

https://doi.org/10.1021/jacs.3c04613
J. Am. Chem. Soc. 2023, 145, 17265−17273

of the exceptional ODHP activity of h-BN as compared to metal borides.

■ ASSOCIATED CONTENT

Data Availability Statement

All unique surface structures from GCGA searches (in ASE database format) are available at https://doi.org/10.5281/zenodo.8187512.

Supporting Information

The Supporting Information is available free of charge at https://pubs.acs.org/doi/10.1021/jacs.3c04613.

Details of the computational models and global optimization methods; benchmarking of the ^{11}B NMR simulations by DFT; surface phase diagram of the h-BN zigzag edge; geometries of the accessible surface phases of restructured h-BN edges; ensemble-based simulation of ^{11}B SSNMR spectra for the h-BN zigzag edge; statistics of key geometric and electronic properties from AIMD simulation; importance of the top features in the trained random forest models; note on the choice of chemical potentials in the GCGA searches; and note on the ML descriptors (PDF)

■ AUTHOR INFORMATION

Corresponding Author

Anastassia N. Alexandrova − *Department of Chemistry and Biochemistry, Department of Materials Science and Engineering, and California NanoSystems Institute, University of California, Los Angeles, Los Angeles, California 90095, United States;* orcid.org/0000-0002-3003-1911; Email: ana@chem.ucla.edu

Authors

Zisheng Zhang − *Department of Chemistry and Biochemistry, University of California, Los Angeles, Los Angeles, California 90095, United States;* orcid.org/0000-0002-4370-4038

Ive Hermans − *Department of Chemistry and Department of Chemical and Biological Engineering, University of Wisconsin−Madison, Madison, Wisconsin 53706, United States;* orcid.org/0000-0001-6228-9928

Complete contact information is available at: https://pubs.acs.org/10.1021/jacs.3c04613

Notes

The authors declare no competing financial interest.

■ ACKNOWLEDGMENTS

This work is supported by the grant DE-SC0019152 from the U.S. Department of Energy, Office of Science, Basic Energy Science Program. The computations in this work were performed on Hoffman2 the UCLA-shared cluster; Cori and Perlmutter of the National Energy Research Scientific Computing Center (NERSC), a U.S. Department of Energy Office of Science User Facility operated under Contract DE-AC02-05CH11231; Theta of the Innovative and Novel Computational Impact on Theory and Experiment (INCITE) program at the Argonne Leadership Computing Facility, a U.S. Department of Energy Office of Science User Facility operated under Contract DE-AC02-06CH11357. We thank Winston Gee, Harry W. T. Morgan, and Melissa Cendejas for helpful discussions.

■ REFERENCES

(1) Sattler, J. J. H. B.; Ruiz-Martinez, J.; Santillan-Jimenez, E.; Weckhuysen, B. M. Catalytic Dehydrogenation of Light Alkanes on Metals and Metal Oxides. *Chem. Rev.* **2014**, *114*, 10613−10653.

(2) Grant, J. T.; Venegas, J. M.; McDermott, W. P.; Hermans, I. Aerobic Oxidations of Light Alkanes over Solid Metal Oxide Catalysts. *Chem. Rev.* **2018**, *118*, 2769−2815.

(3) Grant, J. T.; Carrero, C. A.; Goeltl, F.; Venegas, J.; Mueller, P.; Burt, S. P.; Specht, S. E.; McDermott, W. P.; Chieregato, A.; Hermans, I. Selective Oxidative Dehydrogenation of Propane to Propene Using Boron Nitride Catalysts. *Science* **2016**, *354*, 1570−1573.

(4) Grant, J. T.; McDermott, W. P.; Venegas, J. M.; Burt, S. P.; Micka, J.; Phivilay, S. P.; Carrero, C. A.; Hermans, I. Boron and Boron-Containing Catalysts for the Oxidative Dehydrogenation of Propane. *ChemCatChem* **2017**, *9*, 3623−3626.

(5) Altvater, N. R.; Dorn, R. W.; Cendejas, M. C.; McDermott, W. P.; Thomas, B.; Rossini, A. J.; Hermans, I. B-MWW Zeolite: The Case Against Single-Site Catalysis. *Angew. Chem., Int. Ed. Engl.* **2020**, *59*, 6546−6550.

(6) Zhang, Z.; Zandkarimi, B.; Alexandrova, A. N. Ensembles of Metastable States Govern Heterogeneous Catalysis on Dynamic Interfaces. *Acc. Chem. Res.* **2020**, *53*, 447−458.

(7) Zhang, Z.; Jimenez-Izal, E.; Hermans, I.; Alexandrova, A. N. Dynamic Phase Diagram of Catalytic Surface of Hexagonal Boron Nitride under Conditions of Oxidative Dehydrogenation of Propane. *J. Phys. Chem. Lett.* **2019**, *10*, 20−25.

(8) Venegas, J. M.; Zhang, Z.; Agbi, T. O.; McDermott, W. P.; Alexandrova, A.; Hermans, I. Why Boron Nitride Is Such a Selective Catalyst for the Oxidative Dehydrogenation of Propane. *Angew. Chem., Int. Ed.* **2020**, *59*, 16527−16535.

(9) Zhang, Z.; Tian, J.; Wu, X.; Surin, I.; Pérez-Ramírez, J.; Hemberger, P.; Bodi, A. Unraveling Radical and Oxygenate Routes in the Oxidative Dehydrogenation of Propane over Boron Nitride. *J. Am. Chem. Soc.* **2023**, *145*, 7910−7917.

(10) Love, A. M.; Thomas, B.; Specht, S. E.; Hanrahan, M. P.; Venegas, J. M.; Burt, S. P.; Grant, J. T.; Cendejas, M. C.; McDermott, W. P.; Rossini, A. J. Probing the Transformation of Boron Nitride Catalysts under Oxidative Dehydrogenation Conditions. *J. Am. Chem. Soc.* **2018**, *141*, 182−190.

(11) Hammer, B.; Hansen, L. B.; Nørskov, J. K. Improved Adsorption Energetics within Density-Functional Theory Using Revised Perdew-Burke-Ernzerhof Functionals. *Phys. Rev. B* **1999**, *59*, 7413.

(12) Kresse, G.; Joubert, D. From Ultrasoft Pseudopotentials to the Projector Augmented-Wave Method. *Phys. Rev. B* **1999**, *59*, 1758.

(13) Kresse, G.; Furthmüller, J. Efficiency of Ab-Initio Total Energy Calculations for Metals and Semiconductors Using a Plane-Wave Basis Set. *Comput. Mater. Sci.* **1996**, *6*, 15−50.

(14) Kresse, G.; Furthmüller, J. Efficient Iterative Schemes for Ab Initio Total-Energy Calculations Using a Plane-Wave Basis Set. *Phys. Rev. B* **1996**, *54*, 11169−11186.

(15) Kresse, G.; Hafner, J. Ab Initio Molecular Dynamics for Liquid Metals. *Phys. Rev. B* **1993**, *47*, 558.

(16) Kresse, G.; Hafner, J. Ab Initio Molecular-Dynamics Simulation of the Liquid-Metal−Amorphous-Semiconductor Transition in Germanium. *Phys. Rev. B* **1994**, *49*, 14251.

(17) Henkelman, G.; Uberuaga, B. P.; Jónsson, H. A Climbing Image Nudged Elastic Band Method for Finding Saddle Points and Minimum Energy Paths. *J. Chem. Phys.* **2000**, *113*, 9901−9904.

(18) Smidstrup, S.; Pedersen, A.; Stokbro, K.; Jónsson, H. Improved Initial Guess for Minimum Energy Path Calculations. *J. Chem. Phys.* **2014**, *140*, 214106.

(19) Yu, M.; Trinkle, D. R. Accurate and Efficient Algorithm for Bader Charge Integration. *J. Chem. Phys.* **2011**, *134*, 64111.

(20) Zhai, H.; Alexandrova, A. N. Ensemble-Average Representation of Pt Clusters in Conditions of Catalysis Accessed through GPU Accelerated Deep Neural Network Fitting Global Optimization. *J. Chem. Theory Comput.* **2016**, *12*, 6213−6226.

(21) Deaven, D. M.; Ho, K.-M. Molecular Geometry Optimization with a Genetic Algorithm. *Phys. Rev. Lett.* **1995**, *75*, 288.
(22) Pedregosa, F.; Varoquaux, G.; Gramfort, A.; Michel, V.; Thirion, B.; Grisel, O.; Blondel, M.; Prettenhofer, P.; Weiss, R.; Dubourg, V. Scikit-Learn: Machine Learning in Python. *J. Mach. Learn. Res.* **2011**, *12*, 2825−2830.
(23) Love, A. M.; Thomas, B.; Specht, S. E.; Hanrahan, M. P.; Venegas, J. M.; Burt, S. P.; Grant, J. T.; Cendejas, M. C.; McDermott, W. P.; Rossini, A. J.; Hermans, I. Probing the Transformation of Boron Nitride Catalysts under Oxidative Dehydrogenation Conditions. *J. Am. Chem. Soc.* **2019**, *141*, 182−190.
(24) Wexler, R. B.; Qiu, T.; Rappe, A. M. Automatic Prediction of Surface Phase Diagrams Using Ab Initio Grand Canonical Monte Carlo. *J. Phys. Chem. C* **2019**, *123*, 2321−2328.

https://doi.org/10.1021/jacs.3c04613
J. Am. Chem. Soc. 2023, 145, 17265−17273